Origin of defects induced large flexoelectricity in ferroelectric ceramics

Liangbin Zhang,[1] Zhiguo Wang,[1] Shengwen Shu,[2] Yongming Hu,[3] Chunchun Li ⓘ,[4,5] Shanming Ke,[1]
Fei Li ⓘ,[5] and Longlong Shu ⓘ[1,*]

[1]*School of Materials Science and Engineering, Nanchang University, Nanchang 330031, People's Republic of China*
[2]*College of Electrical Engineering and Automation, Fuzhou University, Fuzhou 350108, People's Republic of China*
[3]*Hubei Key Laboratory of Ferro- and Piezoelectric Materials and Devices, Faculty of Physics and Electronic Science,
Hubei University, Wuhan, People's Republic of China*
[4]*College of Materials Science and Engineering, Guilin University of Technology, Guilin 541004, People's Republic of China*
[5]*Electronic Materials Research Laboratory, Key Laboratory of the Ministry of Education and International Center for Dielectric Research,
Xi'an JiaotongUniversity, Xi'an 710049, People's Republic of China*

Defects have been regarded as playing a critical role in the functionalities of many solid dielectrics. However, the contribution of defects to the specific coupling between strain gradient and electric polarization (i.e., flexoelectricity) has not yet been thoroughly understood. Herein, we selected the typical ferroelectric $BaTiO_3$ (BTO) ceramics and introduced oxygen vacancies and trapped charge defects by using stoichiometric and nonstoichiometric Fe dopants, respectively. Compared with the pure BTO ceramics, the flexoelectric coefficients of stoichiometric Fe-doped BTO ceramics were increased by fivefold (from 9.5 to 65 μC/m) while that of the nonstoichiometric counterparts almost keep stable. The results show that the oxygen vacancies rather than trapped defects make a remarkable contribution to the enhancement of flexoelectricity, and this is explained by the reorientation of the defect dipoles formed by the oxygen vacancies. The result presented in this work not only benefits the understanding of the mechanism of flexoelectricity but also provides a feasible strategy to design flexoelectric materials and related devices with high flexoelectric coefficients.

I. INTRODUCTION

Flexoelectricity is a universal electromechanical coupling effect (strain gradient results in electric polarization) that not only exists in solid dielectrics [1–3], but also in liquid crystals [4,5], semiconductors [6–8], and even metals [9]. This effect has promising application potential in many aspects of cutting edge functional materials, e.g., sensing and actuating, energy storage, memory, and photovoltaics [10–15]. Particularly in oxide thin films and two-dimensional materials, the flexoelectric coupling is extremely significant because strain gradient is inversely proportional to material size [16]. However, from the early stage, since 1964, flexoelectricity had not received much attention for quite a long time due to its much smaller coupling coefficients relative to other well-known electromechanical effects (e.g., piezoelectric coupling) [17]. For most of the materials of which the quantum paraelectric material $SrTiO_3$ single crystal is a representative, the value of flexoelectric coefficients was only in the range of 0.1–1 nC/m [18,19], which highly limits the integration of flexoelectricity into real device applications.

Under such a circumstance, achieving a high flexoelectric coefficient through material design is of the utmost importance for the flexoelectric community. Up until now, several feasible strategies have been proposed. For example, (i) for electrets, introducing neutral charges to promote charge separation could result in two orders of magnitude enhancement of flexoelectric coefficients [20]; (ii) for semiconductors, improving the surface piezoelectricity by increasing carrier density or adding illumination could result in —four to six orders of magnitude enhancement of flexoelectric coefficients [7,21], while for solid dielectrics, the strategy remains unclear. In our previous work, we phenomenologically proved that introducing defects through doping could remarkably improve the flexoelectric coefficients of solid dielectrics [22]. In this context, we examine whether this approach is also valid for bulk ferroelectrics or is just only exclusive for linear dielectrics. Do any types of defects efficiently contribute to the enhanced flexoelectricity and what is the mechanism underlying the defect-enhanced flexoelectricity?

Herein, to address this issue, we selected the classic ferroelectric material $BaTiO_3$ (BTO) ceramics and generated defects by replacing Ti^{4+} (0.604 Å) with low-valence Fe^{3+} (0.55 Å) with a similar radius [23]. The selection of this kind of material is based on the flexoelectricity of BTO ceramics that are fully studied. Furthermore, in order to understand the mechanism of flexoelectricity on defect types, we provided a detailed comparison between stoichiometric doping and nonstoichiometric doping in view of the enhancement of flexoelectricity.

II. EXPERIMENT

A. Materials synthesis

BTO ceramics with $x = 0.2$ mol % Fe dopants were synthesized by the solid-state reaction route using high-purity

*llshu@ncu.edu.cn

$BaCO_3$ (AR, $\geqslant$99.95%, Aladdin, Shanghai, China), TiO_2 (AR, $\geqslant$99.99%, Aladdin, Shanghai, China), and Fe_2O_3 (AR, $\geqslant$99%, Aladdin, Shanghai, China).

The mechanism of Fe-doped BTO ceramics through stoichiometric ratios (xFe-BTO) can be directly reflected in the chemical formula

$$BaCO_3 + (1 - x)TiO_2 + (x/2)Fe_2O_3$$
$$\rightarrow Ba(Ti_{1-x}Fe_x)O_{3-x/2} + CO_2. \qquad (1)$$
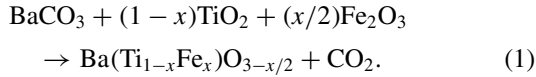
In addition, Fe-doped BTO ceramics through nonstoichiometric ratios ($4x/3$Fe-BTO) were prepared; their chemical expression is

$$BaCO_3 + (1 - x)TiO_2 + (2x/3)Fe_2O_3$$
$$\rightarrow Ba(Ti_{1-x}Fe_{4x/3})O_3 + CO_2. \qquad (2)$$
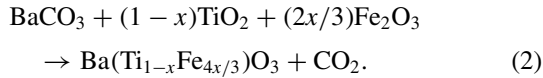
Then ball milling is applied to uniformly mix the weighted powders at 200 rev/min with ethanol as the milling medium. The mixed slurries are dried and prefired at 1000 °C for 6 h, followed by a second ball milling at the same condition, and then they are dried, granulated with polyvinyl alcohol binder (5.0 wt. %), and sieved. Then, under a pressure of about 50 MPa, an isostatic press is used to shape cube blocks with a side length of 20 mm. Further, the green body is placed in a high-temperature furnace sintering at 1300 °C for 6 h. Finally, the bulk specimen is cooled down to room temperature at a rate of 3 °C/min. Moreover, a secondary annealing process (800 °C/3 h) is carried out in a tube furnace under an air atmosphere.

B. Characterization

For the exploration of phase composition and structure, x-ray profiles of Fe-BaTiO$_3$ are recorded at room temperature using a Rigaku Smartlab x-ray diffraction (XRD) diffractometer with Cu $K\alpha$ radiation ($\lambda = 1.5418$ Å). The microscopic morphology and grain size of the Fe-BTO samples are obtained from a scanning electron microscope (SEM) (Gemini SEM 300, Zeiss, Germany). The dielectric properties of the ceramics are measured by a broadband dielectric spectrometer (DMS3000, Partulab, Germany) and an impedance analyzer (E4294A, Palo Alto, USA). The Raman spectrum is measured by a Raman spectrometer (alpha300R, WITec, Germany). The thermally stimulated depolarization current (TSDC) of the ceramic pellets is measured using a pA meter (6517B, Keithley, Cleveland, OH), and a temperature controller (SPIV17T-843F, PK, USA) for temperature dependence measurements. The procedure is to heat the samples to a polarization temperature (T_p) of 80 °C, apply 100–500 V/mm dc polarization field (E_p), and polarize for 20 min. Then, the samples were rapidly cooled to −50 °C (T_0), while maintaining the electric field. Removing the E_p, the samples were short circuited for more than 5 min. Finally, the sample was heated to 200 °C at a constant heating rate of 3 °C/min and the depolarization current was measured. The electron paramagnetic resonance spectroscopy (EPR) is measured using a Bruker EMX Plus electron paramagnetic resonance spectrometer. The spectrometer operates at the X-band frequency (9.30 GHz), 3200 GHz center field, equipped with 100 kHz modulation frequency. The x-ray photoelectron spectroscopy (XPS) is measured by

an x-ray photoelectron spectrometer (K-Alpha, Thermo Scientific, USA).

C. Determination of flexoelectric coefficient

The flexoelectric coefficients were measured through a dynamic thermomechanical analysis system (DMA850, TA Instruments, USA). We used a dynamic mechanical analyzer (DMA) to deliver an oscillatory bending. According to the natural plane assumption of the beam, the bending causes the material to be stretched above the neutral plane, and compressed under the neutral plane. That results in a strain gradient uniformly distributed along the thickness of the cantilever beam.

The strain gradient in a cantilever system can be written as

$$\frac{\partial \varepsilon_{11}}{\partial x_3} = \frac{3w(L)}{L^2}\Big(1 - \frac{x}{L}\Big), \qquad (3)$$

where $w(L)$ is the vertical deflection defection delivered by the piezoelectric actuator at the end of the cantilever, L is the length of the cantilever, and x is the horizontal position along the cantilever.

The relationship between polarization intensity and strain gradient can be expressed as

$$P_3 = \mu_{eff} \frac{\partial \varepsilon_{11}}{\partial x_3}, \qquad (4)$$

where μ_{eff} is the effective flexoelectric coefficient. P_3 is the polarization, and can be obtained by the total electric charge collected on the electrode:

$$P_3 = \frac{Q}{A}, \qquad (5)$$

where Q is the charge measurement by a lock-in amplifier, and A is the electrode area.

III. RESULTS

A. Crystal structure characterization

To manifest the influences of Fe^{3+} dopants on the crystal structure of $BaTiO_3$, variations in the macroscopic structure, local structure, and microstructure were characterized in terms of XRD, Raman spectroscopy, and SEM analysis. Figures 1(a) and 1(b) show the XRD patterns and the corresponding Rietveld refinement of three samples. By analogy, all compositions crystallize into a tetragonal perovskite structure, as characterized by the splitting (002/200) peaks [in the inset of Fig. 1(b)] [24]. Within the detection precision of XRD, no diffraction peaks from the second phase can be detected, which explains the solid solution of the substituted Fe^{3+} in both cases. The decrease in lattice parameter (Table I) provides more evidence for the solid solution because of the smaller ionic radius of Fe^{3+} (0.55 Å, C.N. = 6) compared to Ti^{4+} (0.604 Å, C.N. = 6) the C.N. is defined as the coordination number. It is of primary importance that either stoichiometric or nonstoichiometric doping leads to a limited change in the macroscopic structure.

Raman scattering reflects the vibration or rotation of molecular groups, so it is sensitive to local structural evolution [25]. The Raman active mode of the tetragonal phase BTO can be expressed by the integrable condition:
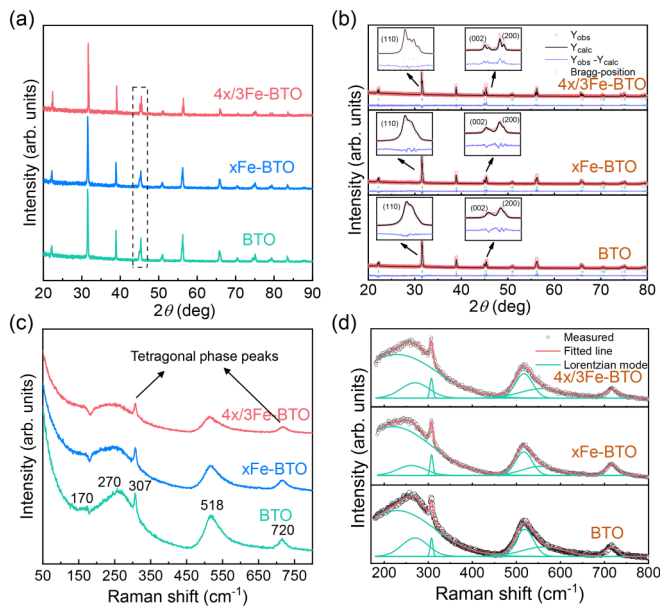
FIG. 1. (a) The room-temperature XRD pattern of Fe-doped BTO ceramics; (b) Rietveld refinement plots for Fe-doped BTO ceramics; (c) Raman spectroscopy of Fe-doped BTO ceramics; and (d) the deconvolution fitting for Fe-doped BTO ceramics.

$\Gamma = 3[A_1(\mathrm{TO}) + A_1(\mathrm{LO})] + B_1 + 4[E(\mathrm{TO}) + E(\mathrm{LO})]$. As illustrated in Fig. 1(c), the dominant features in the spectrum of the three materials are a weak peak at 170 cm^{-1} [A_1(TO)], a broad peak centered near 250 cm^{-1} [A_1(TO)], a sharp peak at 307 cm^{-1} [B_1, E(TO + LO)], an asymmetric and broad peak near 515 cm^{-1} [A_1(TO), E(TO)], and a broad peak at around 720 cm^{-1} [A_1(LO), E(LO)], which is consistent with the previous report [26,27]. The vibrational mode at 307 cm^{-1} stemming from the asymmetry of the [TO$_6$] octahedron confirms the tetragonal symmetry. By deconvoluting using the Gauss-Lorentz function [Fig. 1(d)], no obvious difference is observed based on similar spectra and limited variation in Raman shift as listed in Table II. However, in terms of the full width at half maximum (FWHM), local structure evolution is evident, as characterized by the broadening Raman modes in both Fe-doped samples as compared to the nominal BaTiO$_3$. In general, the local cation disorder of the material is directly correlated with FWHM [28]. As a result, the larger FWHM in the doped samples accounts for the local cation disorder, which might be related to the incorporation of the dopants and the generated lattice defects [29,30].

As recorded in Fig. 2, SEM images show dense microstructures with uniform grains in similar morphology, which

TABLE I. Crystallographic parameters after Rietveld refinement of the XRD pattern of Fe-doped BaTiO$_3$ ceramics.

Samples	Lattice parameters (Å)		R factors (%)		
	$a = b$	c	R_p	R_{wp}	R_{expt}
BTO	3.99652(1)	4.03020(2)	7.29	10.2	4.19
xFe-BTO	3.99619(4)	4.02700(1)	7.19	9.86	3.89
4x/3Fe-BTO	3.99641(6)	4.02894(1)	6.82	9.48	3.81

TABLE II. Optical phonon frequencies (ω) and their mode symmetry assignments and FWHM in Fe-doped BaTiO$_3$.

Symmetry	Samples	ω (cm^{-1})	FWHM
A_1 (TO)	BTO	270	70.61
	xFe-BTO	270	73.87
	4x/3Fe-BTO	270	75.59
B_1, E(LO + TO)	BTO	307	7.09
	xFe-BTO	307	7.79
	4x/3Fe-BTO	307	7.88
A_1(TO), E(TO)	BTO	519	46.29
	xFe-BTO	517	46.54
	4x/3Fe-BTO	517	46.62
A_1(LO), E(LO)	BTO	719	32.16
	xFe-BTO	717	33.30
	4x/3Fe-BTO	717	36.30

further confirms the unity of the phase structure. It is noteworthy that the average grain size for the nominal BTO is $\sim$15.03 and $\sim$21.76 μm for xFe-BTO, but the 4x/3Fe-BTO sample exhibits a much smaller size ($\sim$8.55 μm). It is well accepted that the presence of oxygen vacancies promotes sintering; however, defects that aggregate around grains would inhibit grain growth [31,32]. As a consequence, the difference in grain size is considered to be related to defect types, which will be discussed in detail in the following section.

B. Electrical performance characterization

To manifest the influence of Fe^{3+} dopants on the dielectric behavior of BTO ceramics, the temperature dependence of dielectric constant (ε_r) and loss tangent (tanδ) were recorded in a broad temperature range (30 °C–600 °C). As shown in Fig. 3, over the temperature range (30 °C–150 °C), one sharp dielectric anomaly is observed, which corresponds to the ferroelectric-paraelectric phase transition. Compared to the nominal BTO material ($T_C \sim$ 132 °C), the phase transition temperature of the Fe-doped BTO ceramic is slightly shifted towards the lower temperature ($T_C \sim$ 126 °C for xFe-BTO, and $T_C \sim$ 124 °C for 4x/3Fe-BTO, respectively). Such a variation in T_C value reflects the solid solution of Fe into the lattice of the parent BaTiO$_3$, being consistent with the XRD analysis.

The similar dielectric curves [Figs. 3(a)–3(c)] reveal the minimal influence of Fe^{3+} dopants on the ferroelectric state of BTO ceramics. By contrast, an obvious difference is demonstrated in the paraelectric state, as shown in Figs. 3(d)–3(f) for the high-temperature dielectric curves. A common feature is an abnormal rise in permittivity at elevated temperatures, but with a notably different gradient. A "Δ" term, defined as the magnitude difference in permittivity at 200 °C and 500 °C [$\Delta = \varepsilon_r$(500 °C)–ε_r(200 °C)] is introduced to evaluate the difference. Compared to the nominal BTO ceramic, both xFe-BTO and 4x/3Fe-BTO ceramic exhibit a stronger high-temperature dielectric anomaly, with Δ values several times higher than that of the BTO. Such high-temperature dielectric anomalies have been widely observed in titanates [33] and have been well explained by the defect dipoles that are thermally activated at elevated temperatures [34].
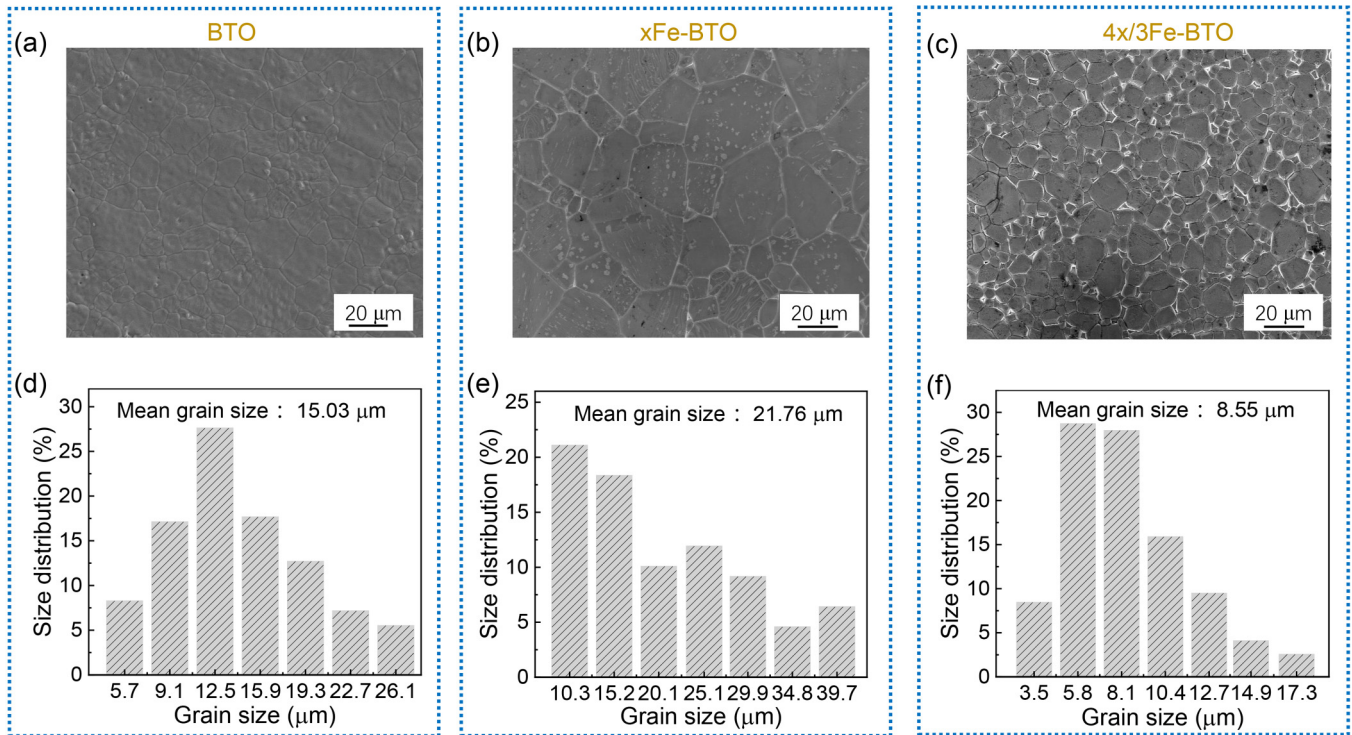
FIG. 2. (a)–(c) The SEM images for Fe-doped BTO ceramics; (d)–(f) the mean grain size map for Fe-doped BTO ceramics.

To comprehensively understand the defects (e.g., defect type and concentration) in the three targeted materials, complex impedance analysis was adopted due to its ability to separate the electric contribution from bulk and interfaces (i.e., grain boundaries and bulk-electrodes interfaces).

Figures 4(a)–4(c) show the complex-plane impedance plot (Z^* plot) of BTO, xFe-BTO, and 4x/3Fe-BTO ceramics at 400 °C–500 °C, respectively. The impedance spectrum of all ceramic samples consists of a large semicircular arc at low frequency and a small arc at high frequency (the inset
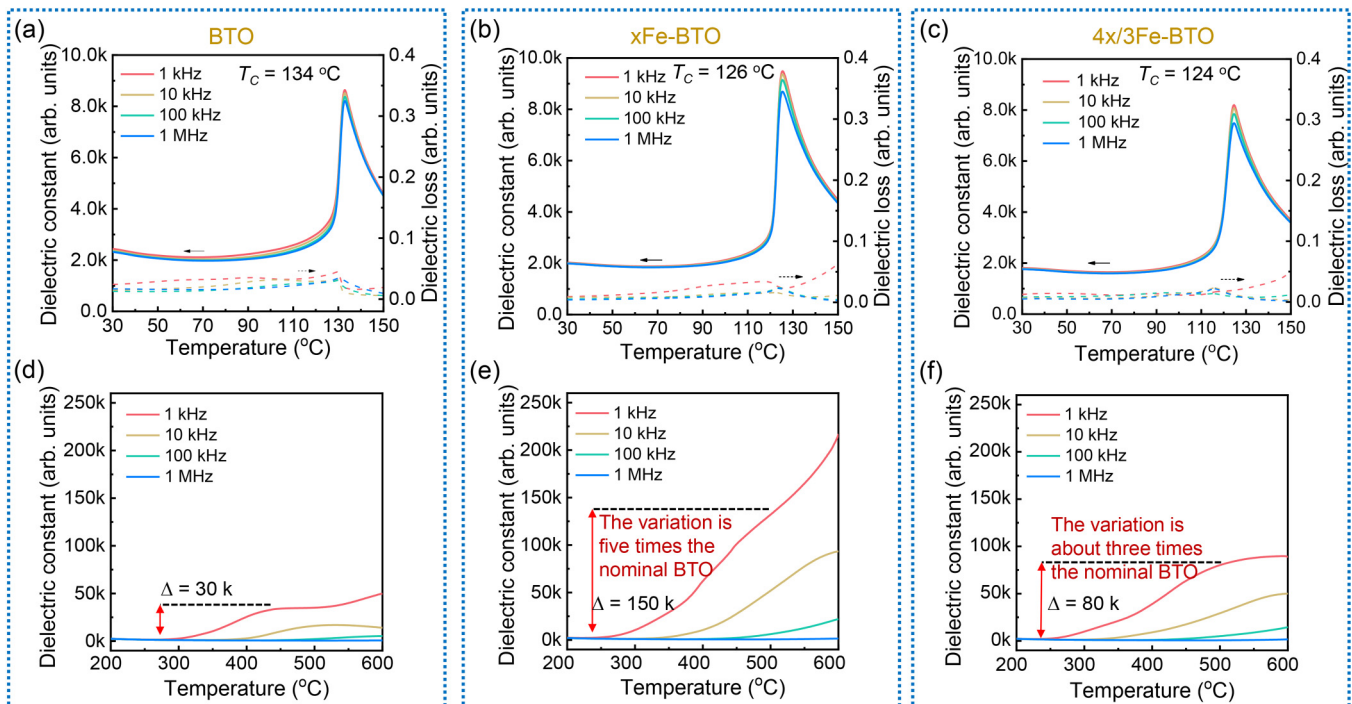
FIG. 3. (a)–(c) Temperature dependence of the dielectric permittivity and dielectric loss in the Fe-BaTiO$_3$ ceramics; (b)–(d): the dielectric constant susceptibility of Fe-doped BTO as a function of high temperature for various frequencies.
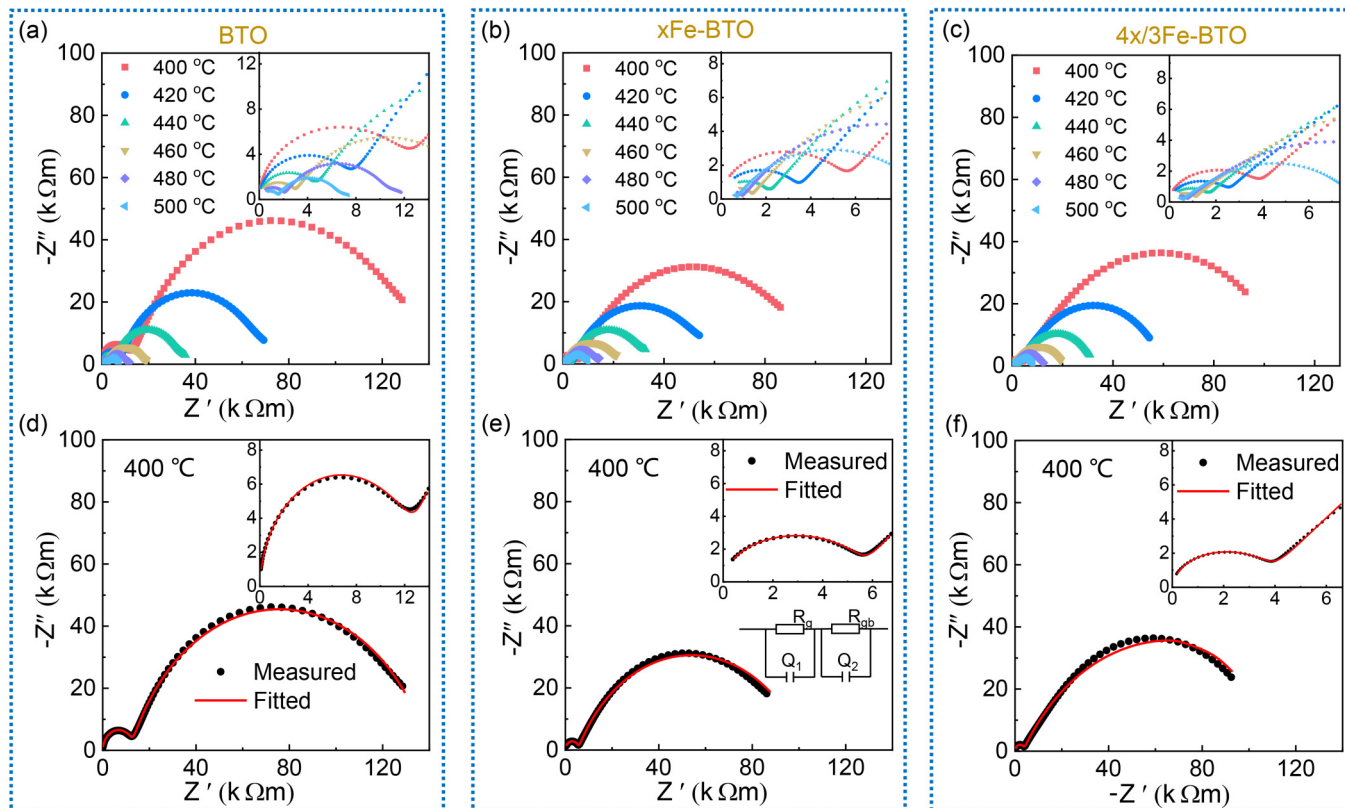
FIG. 4. Z^* plot of (a) BTO, (b) xFe-BTO, and (c) $4x/3$Fe-BTO ceramics as a function of temperature. Complex-plane impedance plots for (d) BTO (e) xFe-BTO, and (f) $4x/3$Fe-BTO ceramics at 400 °C with Z-VIEW fitting results. Illustration in (e) shows an equivalent circuit for the ceramic samples.

shows a magnified view at high frequency). As shown in Figs. 4(d)–4(f), an equivalent circuit consisting of two parallel RC elements in series [see illustration in Fig. 4(e)] is proposed to simulate the impedance response at 400 °C. The constant phase elements (CPEs) rather than the capacitors (C) are used in the equivalent circuit. This is due to nonideal contact between electrode and material, which leads to the nonideal Debye relaxation [35]. Based on the equivalent circuits, the resistances (R) and capacitances (C) can be estimated by using Z-VIEW software, as shown in Table III. For ferroelectric BTO materials, the magnitude of the capacitance is usually used as a basis for assigning the obtained R and C values. It is contributed by grains in the high-frequency semiarc ($\sim$100 pF, for ferroelectric BTO), and contributed by the grain boundary in the low-frequency semiarc ($\sim$10 nF, for ferroelectric BTO) [36]. Compared with the pure BTO ceramic, for Fe-doped BTO ceramics (either stoichiometric or nonstoichiometric doping), the grain resistances are reduced by more than 50%, while the effect on grain boundary resistances is negligible.

The significant variation in grain resistances (rather than grain boundary resistances) indicates the formation of defects in Fe-doped BTO ceramics, and the defects mainly exist in the crystal lattice.

Thermally stimulated depolarization current (TSDC) is measured to further verify the defects and explore the existence form of defects in the matrix [37]. In general, the semiquantitative information of the types (such as trap charges, defect dipoles, and space charges), and concentrations of defects can be distinguished by TSDC via the correlation between polarization field (E_P) and peak position (T_m) and temperature (T_P) [38]. The TSDC curves of BTO, xFe-BTO, and $4x/3$Fe-BTO ($x = 0.2\%$) ceramics are plotted in Fig. 5.

From Fig. 5, an identical feature can be found in the TSDC curve spectrum of all samples, namely, a sharp peak around room temperature and Curie temperature, which is caused by shell and core phase transitions [38,39]. For BTO ceramic [Fig. 5(a)], there are only two TSDC peaks at room

TABLE III. Z-VIEW software fitting results of impedance equivalent circuit for Fe-doped BaTiO$_3$ ceramics at 400 °C.

Samples	Grain resistance (Ω)	Grain capacitance (F)	Grain boundary resistance (Ω)	Grain boundary capacitance (F)
BTO	$12\,093 \pm 45$	$9.86 \times 10^{-11} \pm 2.5 \times 10^{-12}$	$127\,290 \pm 558$	$3.04 \times 10^{-8} \pm 5.6 \times 10^{-10}$
xFe-BTO	5333 ± 20	$7.40 \times 10^{-11} \pm 3.0 \times 10^{-12}$	$117\,260 \pm 505$	$9.17 \times 10^{-8} \pm 1.5 \times 10^{-9}$
$4x/3$Fe-BTO	3627 ± 33	$8.65 \times 10^{-11} \pm 6.9 \times 10^{-12}$	$121\,510 \pm 1543$	$1.65 \times 10^{-7} \pm 4.5 \times 10^{-9}$
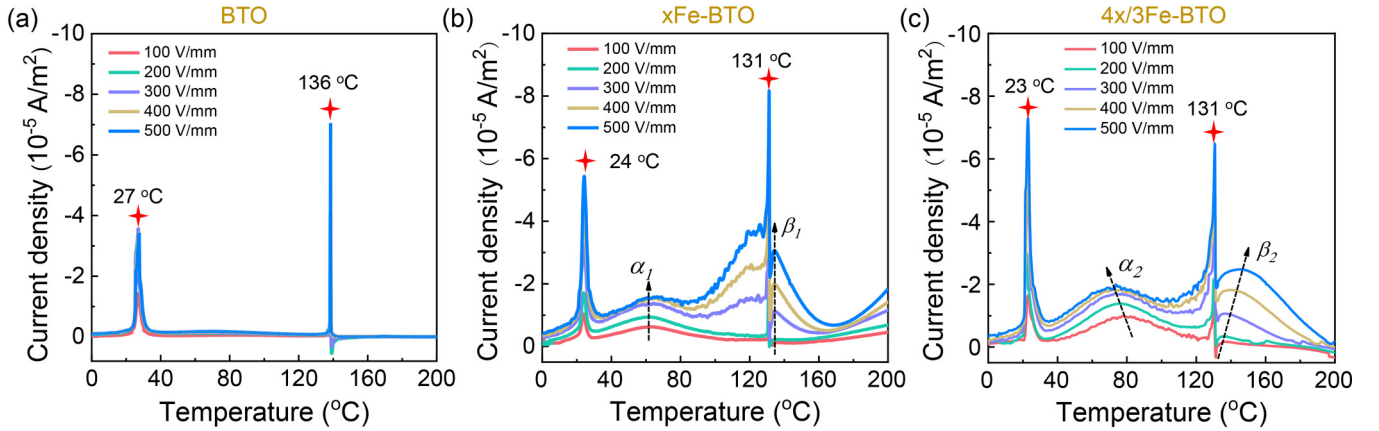
FIG. 5. TSDC spectra for Fe-doped BTO ceramics with different polarization field: (a) BTO, (b) xFe-BTO, and (c) $4x/3$ Fe-BTO.

temperature and Curie temperature, which are due to the sparse defect concentration [40]. for xFe-BTO ceramic, as shown in Fig. 5(b), the spectrum shows two other TSDC peaks, marked as α peaks ($\sim$60 °C) and β peaks ($\sim$135 °C). Regardless of the polarization field E_P, the peak temperatures T_m of the α_1 and β_1 peaks remain almost constant but their maximum increases continuously with increasing dc fields. In contrast, different TSDC behaviors are observed for the $4x/3$ Fe-BTO sample, as shown in Fig. 5(c). The two dc field-dependent TSDC peaks appear around 80 °C (α_2) and 140 °C (β_2), respectively. The TSDC peak around 80 °C is characterized by decreasing peak temperature and increasing peak magnitude with increasing polarization field. In addition, the other TSDC peak around 140 °C is characterized by increasing peak temperature and increasing peak magnitude with increasing polarization field. The differences in the TSDC behavior for different samples demonstrate the differences in defect types, which will be further identified in subsequent discussions.

XPS was employed to further evaluate the generation of oxygen vacancies in Fe-doped BTO ceramics. The O $1s$ XPS spectra [Figs. 6(a)–6(c)] of Fe-doped BTO can be fitted by the Lorentz-Gaussian function to obtain three fitted peaks (peaks I–III). The peak at $\sim$529 eV is caused by the O ions inherent in the BTO lattice (peak I), while the oxygen vacancy, bound water, and the surface hydroxyl group contribute to the two peaks at $\sim$531 eV (peak III) and $\sim$532 eV (peak II), respectively [41]. The percentages of oxygen vacancies in the BTO, xFe-BTO, and $4x/3$Fe-BTO samples are calculated to be 0.6%, 2.7%, and 0.4%, respectively. Figures 6(d)–6(f) show the test data and fitting results of Ti $2p$ orbitals of ceramic samples. Ti $2p_{1/2}$ and Ti $2p_{3/2}$ split into two spin-orbit splitting peaks at $\sim$458 and $\sim$463.7 eV with an energy difference of $\Delta = 5.7$ eV, while two peaks appearing at $\sim$457.3 and $\sim$462.9 eV can indicate the presence of Ti^{3+} [42]. The contents of $V_O^{\bullet\bullet}$ and Ti^{3+} in Fe-doped BTO ceramic samples are recorded in Table IV. The oxygen vacancy concentration in the xFe-BTO ceramic samples would be higher than the nominal BTO and $4x/3$Fe-BTO. The trace oxygen vacancies and the Ti^{4+} to Ti^{3+} transition in the nominal BTO material originate from the partial oxygen detachment from the lattice by high-temperature sintering at standard atmospheric pressure. The

reduction of $V_O^{\bullet\bullet}$ and Ti^{3+} content in $4x/3$Fe-BTO ceramics is attributed to the inhibitory effect of the remaining Fe ions.

To further determine the valence state of the Fe dopants in the samples the EPR spectra of Fe-doped BTO ceramics are characterized and recorded in Fig. 7. The EPR spectrum of the Fe-doped BTO consists of signals with $g \approx 5.639$, 4.445, 4.006, 2.127, 2.002, and 1.888. The g factor is an important piece of information obtained in EPR spectra that can identify specific metal ions and their oxidation states and coordination environments in the measured samples [43,44]. The experimentally observed signal at $g = 1.888$ originates from Ti^{3+} [45]. In addition, the presence of multiple other absorption lines in the experimentally observed spectra is the response of unpaired electrons on the d orbitals of Fe^{3+} to the magnetic field, indicating different environments for Fe^{3+}. Substitution of Fe^{3+} for Ti^{4+} causes changes in the coordination crystal field and different splitting of the d orbital energy levels, exhibiting different resonance peaks [46,47]. Meanwhile, the resonance peaks produced by Fe^{3+} are all unsplit single peaks, which indicates that no other oxidation states are present [48,49].

For ferroelectric materials, during strain gradient application, the ferroelectric dipole breaks the dipole equilibrium and produces considerable net polarization (flexoelectric polarization) along the strain gradient direction, as previously reported in PIN-PMN-PT single crystals [50] and PMN ceramics [51]. In other words, samples exhibiting more superior ferroelectric properties are prone to exhibit a larger flexoelectric response. The polarization–electric field (P-E) hysteresis loops of the Fe-doped BTO ceramics are recorded in Fig. 8. The remanent polarization and coercive field of the samples were recorded in Table V. The remanent polarization

TABLE IV. Oxygen vacancy and Ti^{3+} ion content in Fe-doped BaTiO$_3$ ceramics.

Samples	Oxygen vacancy	Ti^{3+} ion
BTO	0.6%	5.6%
xFe-BTO	2.7%	8.9%
$4x/3$Fe-BTO	0.4%	4.6%
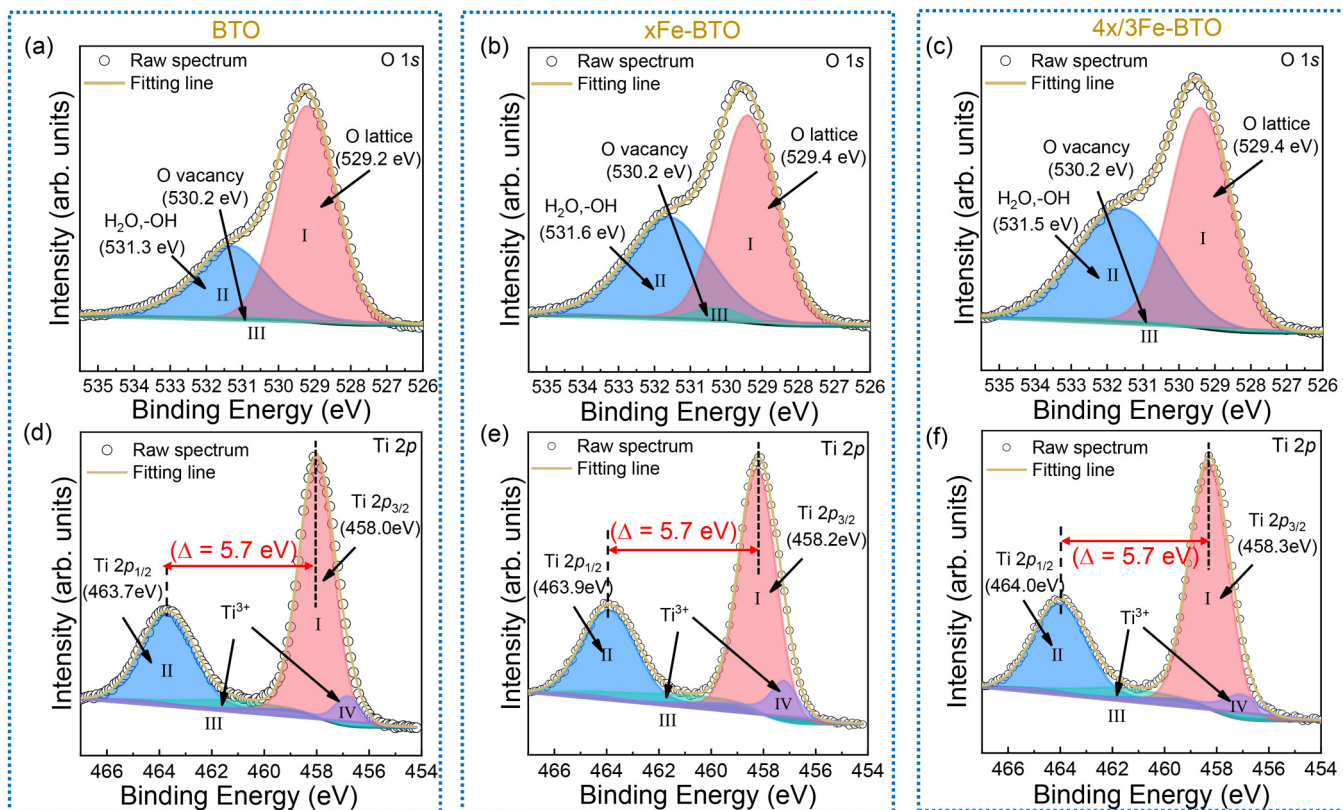
FIG. 6. The O 1s XPS spectra of (a) BTO, (b) xFe-BTO, and (c) 4x/3Fe-BTO, and the Ti 2p XPS spectra of (d) BTO, (e) xFe-BTO, and (f) 4x/3Fe-BTO.

is 8.07, 10.32, and 8.81 $\mu C/cm^2$, and the coercive field is 2.30, 2.93, and 3.14 kV/cm for BTO ceramic, xFe-BTO ceramic, and 4x/3Fe-BTO ceramic. Compared with the nominal BTO, Fe-doped BTO ceramics have larger remanent polarization and coercive field, which indicates that the trace Fe^{3+} dopant improves the ferroelectric properties of BTO ceramics [52].

C. Flexoelectric response

Figure 9(a) shows the relationship between the polarization and the strain gradient of the Fe-doped BTO ceramics. The flexoelectric coefficients obtained by linear fitting are 9.5, 65, and 10.5 $\mu C/m$ for BTO ceramic, xFe-BTO ceramic, and 4x/3Fe-BTO ceramic, respectively. The flexoelectric coefficient of stoichiometric Fe-doped BTO ceramics is 6 times higher than that of BTO ceramics at room temperature. Conversely, the flexoelectric coefficients of 4x/3Fe-BTO ceramics are approximately equal to that of pure BTO ceramics. The test results show that the enhancement of flexoelectric response is closely related to oxygen vacancy.

Figure 9(b) shows the relationship between the flexoelectric coefficient and temperature dependence of Fe-doped BTO ceramics. In the ferroelectric region, a common feature is that the flexoelectric coefficient increases with increasing temperature and peaks at Curie temperature (T_C), which is consistent with the dielectric variation in low-temperature regions. For xFe-BTO, the flexoelectric coefficient is several times higher than that of pure BTO, while the flexoelectric coefficient of

4x/3Fe-BTO is comparable to that of pure BTO. In the paraelectric region, due to the disappearance of ferroelectricity, the flexoelectric coefficients of all ceramics drop sharply and eventually level off. Further, to exclude the direct contribution from the dielectric constant, the flexocoupling coefficients γ of these Fe-doped BTO ceramics are calculated and plotted in Fig. 9(c) [2]. Twenty volts is considered to be the threshold of intrinsic flexoelectricity [53,54], which can be broken by
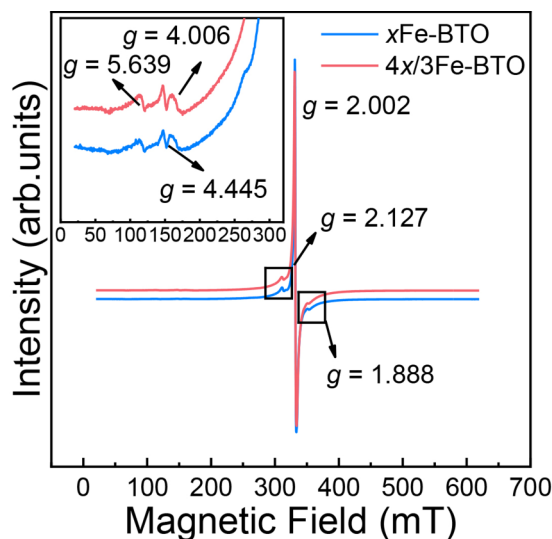
FIG. 7. The EPR spectra for Fe-doped BTO.

TABLE V. The remanent polarization and coercive field for Fe-doped BaTiO$_3$ ceramics.

Samples	Remanent polarization (μC/cm^2)	Coercive field (kV/cm)
BTO	6.23	2.30
xFe-BTO	10.32	2.93
$4x/3$Fe-BTO	8.81	3.14

factors such as ferroelectricity. For xFe-BTO ceramics, the γ is much higher than that of pure BTO ceramics in the ferroelectric phase. In addition, when the Curie temperature is exceeded, the γ is still greater than that of pure BTO, which further proves the enhancement effect of oxygen vacancies on flexoelectricity. This suggests that even without ferroelectricity, flexoelectricity can still be effectively boosted by oxygen vacancies, which is consistent with the phenomenon observed in linear dielectrics [22]. For $4x/3$Fe-BTO ceramics, the γ is at the same level as that of pure BTO ceramic in the paraelectric phase, which indicates that the flexoelectricity is not enhanced by defects created by nonstoichiometric doping. Although there is a slight increase of the γ in the ferroelectric phase, we believe that this is due to the enhancement of ferroelectricity rather than the presence of defects (Fig. 8).

IV. DISCUSSION

In the present system, acceptor doping, for BaTiO$_3$ perovskites, either on the A site (Li$^+$ or K$^+$) or the B site (Fe^{3+}, Mn^{2+}) leads to negatively charged lattice defects (Li$'_{Ba}$ or Fe$'_{Ti}$), which need to be compensated by positively charged defects to maintain the local electroneutrality. Usually, for titanates, ionized oxygen vacancies ($V_O^{\bullet\bullet}$) are rational to offset the acceptor defects [55,56]. For stoichiometric doping, Fe is incorporated as an acceptor at the B site, and the effect of Fe substitution for the Ti ion can be expressed by Kröger-Vink notation as

$$\text{Fe}_2\text{O}_3 \xrightarrow{\text{2BaTiO}_3} 2\text{Fe}'_{\text{Ti}} + V_O^{\bullet\bullet} + 5\text{O}_O + 2\text{Ba}_{\text{Ba}}. \qquad (6)$$
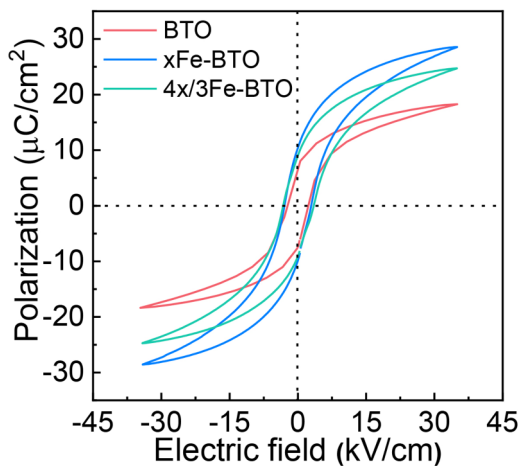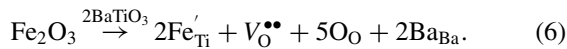
FIG. 8. The hysteresis loop of Fe-doped BTO ceramics at room temperature.

Since the substitution at the B site is low valent (Ti^{4+} is replaced by Fe^{3+}), a positively charged oxygen vacancy is created to balance the local charge imbalance. At this time, the acceptor doped ions and the oxygen vacancy form the defect dipole ($[\text{Fe}'_{\text{Ti}} - V_O^{\bullet\bullet}]^\bullet$) [43,57].

From Eq. (2), compared with the stoichiometric replacement of Fe to Ti to generate oxygen vacancies, in nonstoichiometric doping, more Fe ions will participate in the charge balance process and suppress the appearance of oxygen vacancies [58]. The core goal and rationality of its realization of charge compensation have also been proved [59]. Furthermore, charge defects (point defects) are usually formed in nonstoichiometric compounds [60].

Based on the experimental facts above, a basic question is why stoichiometric doping exhibits a higher flexoelectric response. The flexoelectric properties of materials are affected by several factors, including intrinsic factors and extrinsic defects (such as impurities, porosity, grain boundaries, etc.) [61]. In this paper, crystal structure (external factors) and defect type (internal mechanism) were explored. In the first part of region 3, the results of XRD, Raman, and SEM characterization effectively negate the role of external factors in the present system. The variations in electrical performance (high-temperature dielectric, impedance spectroscopy, and TSDC) shown by the three materials strongly demonstrate the different defect types in Fe-doped BTO samples. Defect dipoles formed in xFe-BTO; the defect form of $4x/3$Fe-BTO is charge defect or trap charge. In the subsequent characterization of flexural electrical properties, BaTi$_{1-x}$Fe$_x$O$_3$ ceramics showed several times higher flexural electrical responses than the other two materials. After excluding the influence of external factors, it was strongly proved that the defect dipole plays a great role in the material flexoelectric response. The main experimental evidence is discussed as follows:

(i) The average grain size of xFe-BTO ceramic is the maximum among the three materials. As previously reported, the increase in oxygen vacancy concentration can induce vacancy or particle flow diffusion, which promotes the mass transfer process and thus promotes sintering. Importantly, this is consistent with theoretical predictions and can serve as a basis for stoichiometric doping to produce oxygen vacancy.

(ii) The pronounced high-temperature dielectric anomaly and variation in impedance of Fe-doped BTO are compared to pure BTO. The high-temperature dielectric anomaly with no association with phase transition has usually been observed in perovskites and is believed to be related to the defect dipoles due to the presence of lattice defects (oxygen vacancies, etc.) [34]. For example, oxygen vacancies facilitate the appearance of dipoles formed with an adjacent host ion, and dipoles respond to the external field by rotation and other ways to participate in the contribution of the dielectric constant. At higher temperatures, the oxygen vacancy will dissociate, and the free oxygen vacancies migrate in a thermally activated state and accumulate at the insulating grain boundaries, triggering an anomalous increase in dielectric behavior and accumulate at the insulating grain boundaries, triggering an anomalous increase in dielectric behavior. Lattice defects generated by Fe^{3+} doping can be qualitatively judged from this.
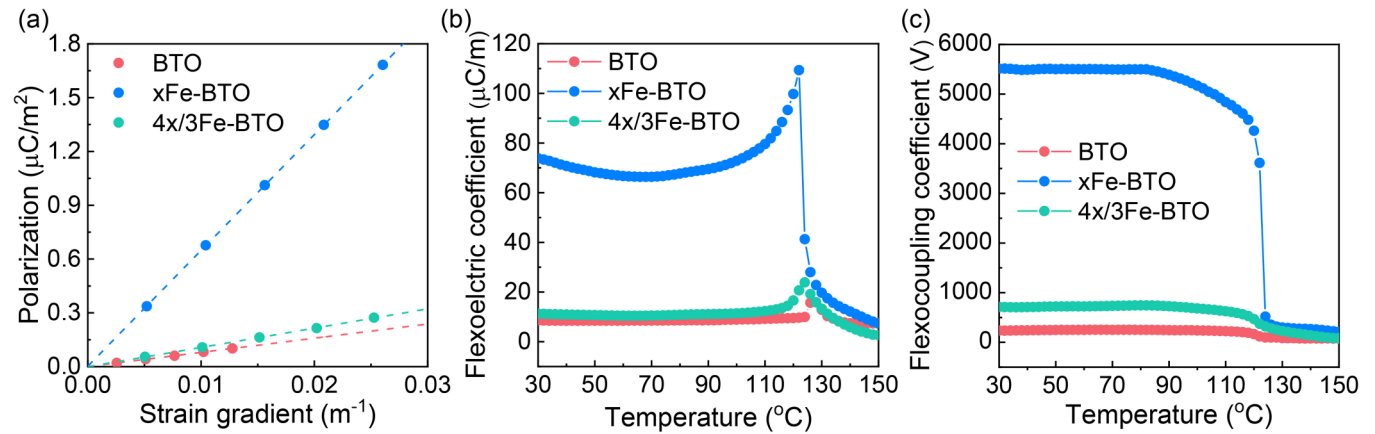
FIG. 9. (a): The room-temperature flexoelectric coefficient for Fe-doped BTO ceramics; (b) the variable temperature flexoelectric coefficient for Fe-doped BTO ceramics; (c) the variable temperature flexoelectric coupling coefficient for Fe-doped BTO ceramics.

For xFe-BTO, oxygen vacancies will be formed, while for $4x/3$Fe-BTO, residual Fe^{3+} may be present in the lattice as interstitial ions.

(iii) A variety of complementary methods, including Raman spectroscopy (Raman), x-ray photoelectron spectroscopy (XPS), electron paramagnetic resonance spectroscopy (EPR), and thermally stimulated depolarization current (TSDC), provide the main evidence for the determination of defect type, defect concentration, etc. For the Raman spectrum, the large difference between the cationic disorder of nominal BTO and Fe-doped BTO ceramics is mainly reflected in the main molecular vibrational modes with $[TiO_6]$ octahedra (around 270 and 307 cm^{-1}), which provides sufficient evidence for Ti substitution by Fe into the BTO lattice. The XPS characterization results demonstrate the presence of oxygen vacancies and also verify the difference in the concentration of oxygen vacancies in the three materials. Meanwhile, it can be learned from the EPR results that the Fe dopants are mainly present in the form of Fe^{3+} in the Fe-doped BTO ceramics, which provides an important judgment for the subsequent determination of the defect type. The TSDC variation of xFe-BTO ceramic recorded above at non–room temperature is inherent to the orientation degree of defect dipoles, corresponding to the $([Fe'_{Ti} - V_O^{\bullet\bullet}]^{\bullet})$ orientation peak [43], which is also observed in $BaTiO_3$-$Bi(Zn_{0.5}Y_{0.5})O_{2.75}$ ceramics [62]. For $4x/3$Fe-doped BTO ceramic, the TSDC peak around $80\,^{\circ}$C is characterized by decreasing peak temperature and increasing peak magnitude with increasing polarization field, which arises from the trapped defects. While the TSDC behavior at $140\,^{\circ}$C arises from the charge or vacancy migration, meantime, combined with the dielectric and impedance behavior of the $4x/3$Fe-doped BTO ceramic, it can be determined that the excess Fe^{3+} is present in the lattice as interstitial ions. The results reflect the difference in the types of defects formed by the two doping methods.

(iv) The flexoelectric coefficient of xFe-BTO ceramics is several times that of the other two materials. From the review of the experimental results, the effect of weak difference in extrinsic factors on flexoelectric response can be judged to be non-dominant. However, the intrinsic mechanism of the huge flexoelectric response of xFe-BTO ceramic is, through

the comparison of different doping modes, explained as the reorientation of defect dipoles under the action of the intrinsic flexoelectric field. A low amount of stoichiometric doping results in oxygen vacancies that are extremely sensitive to the flexoelectric field, and the reorientation of oxygen vacancies in the form of dipoles under a stronger flexoelectric field of ferroelectric materials leads to a huge increase of bending charge [22]. Charge migration and trap charge are generated by the nonstoichiometric method. These defects are less sensitive to the electric field and cause a very weak enhancement to the flexoelectricity. These findings were further verified in the study of the flexoelectric temperature spectrum and the flexoelectric coupling coefficient.

V. CONCLUSIONS

In this paper, we selected the typical ferroelectric ceramics BTO as the representative, and systematically studied the effects of oxygen vacancies (through stoichiometric doping Fe) and trapped charge defects (through nonstoichiometric doping Fe) on flexoelectricity. The results show that the flexoelectricity of the stoichiometric Fe-doped BTO ceramics has a significant improvement, while the flexoelectricity of the nonstoichiometric Fe-doped BTO ceramics is comparable to that of pure BTO. This is attributed to the reorientation of defect dipoles under the flexoelectric field inducing more bending charges, while trapped charge defects do not contribute to the enhancement of flexoelectricity. This work not only benefits the understanding of the mechanism of flexoelectricity but also provides a feasible strategy to design flexoelectric materials and related devices with high flexoelectric coefficients.

[1] A. Biancoli, C. M. Fancher, J. L. Jones, and D. Damjanovic, Breaking of macroscopic centric symmetry in paraelectric phases of ferroelectric materials and implications for flexoelectricity, Nat. Mater. **14**, 224 (2015).

[2] J. Narvaez, S. Saremi, J. W. Hong, M. Stengel, and G. Catalan, Large Flexoelectric Anisotropy in Paraelectric Barium Titanate, Phys. Rev. Lett. **115**, 037601 (2015).

[3] L. L. Shu, X. Y. Wei, T. Pang, X. Yao, and C. L. Wang, Symmetry of flexoelectric coefficients in crystalline medium, J. Appl. Phys. **110**, 104106 (2011).

[4] J. S. Patel and R. B. Meyer, Flexoelectric Electro-Optics of a Cholesteric Liquid-Crystal, Phys. Rev. Lett. **58**, 1538 (1987).

[5] Q. Deng, L. Liu, and P. Sharma, Electrets in soft materials: Nonlinearity, size effects, and giant electromechanical coupling, Phys. Rev. E **90**, 012603 (2014).

[6] J. Narvaez, F. Vasquez-Sancho, and G. Catalan, Enhanced flexoelectric-like response in oxide semiconductors, Nature (London) **538**, 219 (2016).

[7] L. Shu, S. Ke, L. Fei, W. Huang, Z. Wang, J. Gong, X. Jiang, L. Wang, F. Li, S. Lei, Z. Rao, Y. Zhou, R. Zheng, X. Yao, Y. Wang, S. Massimiliano, and C. Gustlan, Photoflexoelectric effect in halide perovskites, Nat. Mater. **19**, 605 (2020).

[8] L. Wang, S. Liu, X. Feng, C. Zhang, L. Zhu, J. Zhai, Y. Qin, and Z. Wang, Flexoelectronics of centrosymmetric semiconductors, Nat. Nanotechnol. **15**, 661 (2020).

[9] A. Zabalo and M. Stengel, Switching a Polar Metal via Strain Gradients, Phys. Rev. Lett. **126**, 127601 (2021).

[10] F. J. Maier, M. Schneider, J. Schrattenholzer, W. Artner, K. Hradil, A. Artemenko, A. Kromka, and U. Schmid, Flexoelectricity in polycrystalline TiO$_2$ thin films, Acta Mater. **190**, 124 (2020).

[11] H. Lu, C. W. Bark, D. Esque de los Ojos, J. Alcala, C. B. Eom, G. Catalan, and A. Gruverman, Mechanical writing of ferroelectric polarization, Science **336**, 59 (2012).

[12] X. Chen, X. Tang, X. Z. Chen, Y. L. Chen, X. Guo, H. X. Ge, and Q. D. Shen, Nonvolatile data storage using mechanical force-induced polarization switching in ferroelectric polymer, Appl. Phys. Lett. **106**, 042903 (2015).

[13] M. M. Yang, D. Kim, and M. Alexe, Flexo-photovoltaic effect, Science **360**, 904 (2018).

[14] B. Wang, H. D. Lu, C. W. Bark, C. B. Eom, A. Gruverman, and L. Q. Chen, Mechanically induced ferroelectric switching in BaTiO$_3$ thin films, Acta Mater. **193**, 151 (2020).

[15] D. Lee, S. M. Yang, J. G. Yoon, and T. W. Noh, Flexoelectric rectification of charge transport in strain-graded dielectrics, Nano Lett. **12**, 6436 (2012).

[16] M. S. Majdoub, P. Sharma, and T. Cagin, Enhanced size-dependent piezoelectricity and elasticity in nanostructures due to the flexoelectric effect, Phys. Rev. B **77**, 125424 (2008).

[17] S. M. Kogan, Piezoelectric effect during inhomogeneous deformation and acoustic scattering of carriers in crystals, Sov. Phys. - Solid State **5**, 2069 (1964).

[18] P. Zubko, G. Catalan, A. Buckley, P. R. Welche, and J. F. Scott, Strain-Gradient-Induced Polarization in SrTiO$_3$ Single Crystals, Phys. Rev. Lett. **99**, 167601 (2007).

[19] L. L. Shu, R. H. Liang, Z. G. Rao, F. Li, S. M. Ke, and Y. Wang, Flexoelectric materials and their related applications: A focused review, J. Adv. Ceram. **8**, 153 (2019).

[20] X. Wen, D. Li, K. Tan, Q. Deng, and S. Shen, Flexoelectret: An Electret with a Tunable Flexoelectriclike Response, Phys. Rev. Lett. **122**, 148001 (2019).

[21] Z. Dai, S. Guo, Y. Gong, and Z. Wang, Semiconductor flexoelectricity in graphite-doped SrTiO$_3$ ceramics, Ceram. Int. **47**, 6535 (2021).

[22] Z. Wang, C. Li, Z. Zhang, Y. Hu, W. Huang, S. Ke, R. K. Zheng, F. Li, and L. Shu, Interplay of defect dipole and flexoelectricity in linear dielectrics, Scr. Mater. **210**, 114427 (2022).

[23] R. D. Shannon, Revised effective ionic radii and systematic studies of interatomic distances in halides and chalcogenides, Acta Crystallogr. **32**, 751 (1976).

[24] R. Asiaie, W. Zhu, S. A. Akbar, and P. K. Dutta, Characterization of submicron particles of tetragonal BaTiO$_3$, Chem. Mater. **8**, 226 (1996).

[25] C. Yin, Z. Yu, L. Shu, L. Liu, Y. Chen, and C. Li, A low-firing melilite ceramic Ba$_2$CuGe$_2$O and compositional modulation on microwave dielectric properties through Mg substitution, J. Adv. Ceram. **10**, 108 (2020).

[26] U. Venkateswaran, V. Naik, and R. Naik, High-pressure Raman studies of polycrystalline BaTiO$_3$, Phys. Rev. B **58**, 14256 (1998).

[27] G. Burns and B. A. Scott, Raman scattering in the ferroelectric system Pb$_{1-x}$Ba$_x$TiO$_3$, Solid State Commun. **9**, 813 (1971).

[28] M. Rakhi and G. Subodh, Crystal structure and microwave dielectric properties of NaPb$_2$B$_2$V$_3$O$_{12}$ (B = Mg, Zn) ceramics, J. Eur. Ceram. Soc. **38**, 4962 (2018).

[29] Y. Shiratori, C. Pithan, J. Dornseiffer, and R. Waser, Raman scattering studies on nanocrystalline BaTiO$_3$ Part I–isolated particles and aggregates, J. Raman Spectrosc. **38**, 1288 (2007).

[30] G. Busca, V. Buscaglia, M. Leoni, and P. Nanni, Solid-state and surface spectroscopic characterization of BaTiO$_3$ fine powders, Chem. Mater. **6**, 955 (1994).

[31] V. Porokhonskyy, L. Jin, and D. Damjanovic, Separation of piezoelectric grain resonance and domain wall dispersion in Pb(Zr,Ti)O$_3$ ceramics, Appl. Phys. Lett. **94**, 212906 (2009).

[32] Z. Xing, L. Jin, T. Wang, Q. Y. Hu, Y. J. Feng, and X. Y. Wei, Electron-induced secondary electron emission properties of MgO/Au composite thin film prepared by magnetron sputtering, J. Electron. Mater. **43**, 3905 (2014).

[33] O. Bidault, P. Goux, M. Kchikech, M. Belkaoumi, and M. Maglione, Space-charge relaxation in perovskites, Phys. Rev. B **49**, 7868 (1994).

[34] C. Ang, Z. Yu, and L. E. Cross, Oxygen-vacancy-related low-frequency dielectric relaxation and electrical conduction in Bi:SrTiO$_3$, Phys. Rev. B **62**, 228 (2000).

[35] S. Cha and Y. Ha, Effects of Mn doping on dielectric properties of Mg-doped BaTiO$_3$, J. Appl. Phys. **100**, 104102 (2006).

[36] J. T. S. Irvine, D. C. Sinclair, and A. R. West, Electroceramics: Characterization by impedance spectroscopy, Adv. Mater. **2**, 132 (1990).

[37] J. Zhang, Y. Zhou, B. Peng, Z. Xie, X. Zhang, Z. Yue, and S. Troiler-McKinstry, Microwave dielectric properties and thermally stimulated depolarization currents of MgF$_2$-doped diopside ceramics, J. Am. Ceram. Soc. **97**, 3537 (2014).

[38] W. Guo, Z. Ma, Y. Luo, Y. Chen, Z. Yue, and L. Li, Structure, defects, and microwave dielectric properties of Al-doped and Al/Nd co-doped Ba$_4$Nd$_{9.33}$Ti$_{18}$O$_{54}$ ceramics, J. Adv. Ceram. **11**, 629 (2022).

[39] X. Zhang, N. Chang, J. Zhang, Y. Zhou, Z. Yue, and L. Li, Low-loss $(1-x)Ba_{0.6}Sr_{0.4}La_4Ti_4O_{15-x}CaTiO_3$ microwave dielectric ceramics with medium permittivity, J. Alloys Compd. **819**, 153011 (2020).

[40] S. H. Yoon, J. S. Park, S. H. Kim, and D. Y. Kim, Thermally stimulated depolarization current analysis for the dielectric aging of Mn and V-codoped $BaTiO_3$ multilayer ceramic capacitor, Appl. Phys. Lett. **103**, 042901 (2013).

[41] S. Kumara, V. S. Rajua, and T. R. N. Kuttyb, Investigations on the chemical states of sintered barium titanate by x-ray photoelectron spectroscopy, Appl. Surf. Sci. **206**, 250 (2003).

[42] M. E. Pilleux, C. R. Grahmann, and V. M. Fuenzalida, Hydrothermal strontium titanate films on titanium: An XPS and AES depth-profiling study, J. Am. Ceram. Soc. **77**, 1601 (1994).

[43] Y. S. Zhao, B. Yang, Y. P. Liu, Y. P. Zhou, Q. Wu, and S. F. Zhao, Capturing carriers and driving depolarization by defect engineering for dielectric energy storage, ACS Appl. Mater. Interfaces **14**, 6547 (2022).

[44] H. Rumpf, H. Modrow, J. Hormes, H. J. Gläsel, E. Hartmann, E. Erdem, R. Böttcher, and K. H. Hallmeier, Preparation of nanocrystalline $BaTiO_3$ characterized by *in situ* x-ray absorption spectroscopy, J. Phys. Chem. B **105**, 3415 (2001).

[45] M. S. Castro, W. Salgueiro, and A. Somoza, Electron paramagnetic resonance and positron annihilation study of the compensation mechanisms in donor-doped $BaTiO_3$ ceramics, J. Phys. Chem. Solids. **68**, 1315 (2007).

[46] N. Pathak, S. K. Gupta, K. Sanyal, M. Kumar, R. M. Kadama, and V. Natarajana, Photoluminescence and EPR studies on Fe^{3+} doped $ZnAl_2O_4$: An evidence for local site swapping of Fe^{3+} and formation of inverse and normal phase, Dalton Trans. **43**, 9313 (2014).

[47] L. X. Zhang, E. Erdem, X. B. Ren, and R. A. Eichel, Reorientation of $[Mn''_{Ti} - V^{\bullet\bullet}_O]^{\times}$ defect dipoles in acceptor-modified $BaTiO_3$ single crystals: An electron paramagnetic resonance study, Appl. Phys. Lett. **93**, 202901 (2008).

[48] P. Jakes, E. Erdem, R. A. Eichel, L. Jin, and D. Damjanovic, Position of defects with respect to domain walls in Fe^{3+}-doped $Pb[Zr_{0.52}Ti_{0.48}]O_3$ piezoelectric ceramics, Appl. Phys. Lett. **98**, 072907 (2011).

[49] E. Erdem, P. Jakes, S. K. S. Parashar, and K. Kiraz, Defect structure in aliovalently-doped and isovalently-substituted $PbTiO_3$ nano-powders, J. Phys.: Condens. Matter **22**, 345901 (2010).

[50] L. L. Shu, T. Li, Z. G. Wang, F. Li, L. F. Fei, Z. G. Rao, M. Ye, S. M. Ke, W. B. Huang, Y. Wang, and X. Yao, Flexoelectric behavior in PIN-PMN-PT single crystals over a wide temperature range, Appl. Phys. Lett. **111**, 162901 (2017).

[51] W. H. Ma and L. E. Cross, Large flexoelectric polarization in ceramic lead magnesium niobate, Appl. Phys. Lett. **79**, 4420 (2001).

[52] W. Li, D. Zhou, and L. Pang, Enhanced energy storage density by inducing defect dipoles in lead free relaxor ferroelectric $BaTiO_3$-based ceramics, Appl. Phys. Lett. **110**, 132902 (2017).

[53] J. W. Hong and D. Vanderbilt, First-principles theory of frozen-ion flexoelectricity, Phys. Rev. B **84**, 180101 (2011).

[54] P. Zubko, G. Catalan, and A. K. Tagantsev, Flexoelectric effect in solids, Annu. Rev. Mater. Res. **43**, 387 (2013).

[55] X. Wang, Y. Huan, Y. Zhu, P. Zhang, W. Yang, P. Li, T. Wei, L. Li, and X. Wang, Defect engineering of BCZT-based piezoelectric ceramics with high piezoelectric properties, J. Adv. Ceram. **11**, 184 (2022).

[56] O. Condurache, I. Turcan, L. Curecheriu, C. Ciomaga, P. Postolache, G. Ciobanu, and L. Mitoseriu, Towards novel functional properties by interface reaction in mixtures of $BaTiO_3$-Fe_2O_3 composite ceramics, Ceram. Int. **43**, 1098 (2017).

[57] F. D. Morrison, D. C. Sinclair, and A. R. West, An alternative explanation for the origin of the resistivity anomaly in La-doped $BaTiO_3$, Int. J. Inorg. Mater. **3**, 1205 (2001).

[58] J. G. Dickson, L. Katz, and R. Ward, Additions and corrections-compounds with the hexagonal barium titanate structure, J. Am. Chem. Soc. **83**, 3026 (1961).

[59] B. Xu, K. B. Yin, J. Lin, Y. D. Xia, and Z. Liu, Room-temperature ferromagnetism and ferroelectricity in Fe-doped $BaTiO_3$, Phys. Rev. B **79**, 134109 (2009).

[60] J. K. Burdett and G. V. Kulkarni, Defect patterns in perovskites, J. Am. Chem. Soc. **110**, 5361 (1988).

[61] L. Shu, M. Wan, Z. Wang, L. Wang, S. Lei, T. Wang, W. Huang, N. Zhou, and Y. Wang, Large flexoelectricity in Al_2O_3-doped $Ba(Ti_{0.85}Sn_{0.15})O_3$ ceramics, Appl. Phys. Lett. **110**, 192903 (2017).

[62] Z. Luo, H. Hao, C. Chen, L. Zhang, Z. Yao, M. Cao, M. Emmanuel, and H. Liu, Dielectric and anti-reduction properties of $(1-x)BaTiO_{3-x}Bi(Zn_{0.5}Y_{0.5})O_{2.75}$ ceramics for BME-MLCC application, J. Alloys Compd. **794**, 358 (2019).